Investigating the activity of modified TiO_2 photocatalysts used for the photoreforming of biomass derivatives

Muhammad Umair[1], Vittorio Loddo[1,*], Leonardo Palmisano[1], Albin Pintar[2], Gregor Žerjav[2], Giovanni Palmisano[3,4], Samar Al Jitan[3,4], Marianna Bellardita[1,*]

[1]Engineering Department, University of Palermo, Viale delle Scienze Ed. 6, Palermo 90128, Italy

[2]Department of Inorganic Chemistry and Technology, National Institute of Chemistry, Hajdrihova 19, SI-1001 Ljubljana, Slovenia

[3]Department of Chemical Engineering, Khalifa University of Science and Technology, P.O. Box 127788, Abu Dhabi, United Arab Emirates

[4]Research and Innovation Center on CO_2 and H_2, Khalifa University of Science and Technology, P.O. Box 127788, Abu Dhabi, United Arab Emirates

[*]Corresponding authors: Prof. Marianna Bellardita (marianna.bellardita@unipa.it); Prof. Vittorio Loddo (vittorio.loddo@unipa.it).

Keywords: Photocatalytic H_2 production; Biomass valorisation; Modified TiO_2; Glucose and fructose partial oxidation

Abstract

Different TiO_2 modified (with Pt, Cu_2O, Nb) photocatalysts have been compared for the photo-reforming of glucose and fructose at ambient conditions with the aim of linking the photoactivity to some structural and surface characteristics. A different degree of conversion, distribution of intermediates and H_2 production were observed with the various photocatalysts. Moreover, the results obtained with the same catalysts were slightly different with the two substrates, highlighting the importance of the interaction between the catalyst surface and the organic compound. Bare TiO_2 was inactive towards H_2 production, Cu_2O was effective in replacing Pt for hydrogen generation, and the presence of Pt/Nb was beneficial for both H_2 production and selective oxidation. Moreover, Pt not only works as a sink for the photoproduced electrons, as it is well known in the literature, but also modifies the surface acid-base properties of catalysts as revealed by DRIFT and TPD measurements.

Introduction

The traditional industrial processes involving the consumption of fossil fuels have a great impact on global warming and environmental pollution [1]. Therefore, the development of new, eco-friendly and clean industrial processes based on the use of renewable energy has emerged as the most pressing challenge for researchers working in the green chemistry field [2]. The transformation of biomass into chemicals is a promising approach to counter the negative impacts caused by the excessive consumption of fossil fuels [3,4]. Natural biomass is a renewable energy source that does not emit greenhouse gases because it is created by plants during photosynthesis from CO_2 and water [5]. Biomass and its derivatives are considered valuable inexpensive raw materials for pharmaceutical, food, cosmetic and fuel industry [5–8]. Furthermore, hydrogen production from biomass is considered a valid alternative to traditional expensive methods. Hydrogen is a clean, affordable, efficient, inexhaustible, storable, and eco-friendly fuel that produces just water when burned, with no pollutants, particulates or greenhouse gases released into the atmosphere [9–11]. Glucose and fructose, which derived from cellulose, can be used to produce high-value compounds in a sustainable mode. In particular, they can be used to make ethanol, mannitol and sorbitol through hydrogenation, 5-hydroxymethyl furfural through dehydration, gluconic acid, arabinose and erythrose by partial oxidation and hydrogen [12–19].

Photocatalysis is an environmentally friendly process used in organic synthesis and pollutant removal [3,20–23]. The use of photocatalysis has several advantages for the environment, including mild operating conditions (i.e. room temperature and ambient pressure), the absence of harmful chemical solvents, the possibility of solar light utilization as irradiation source, the easy integration with other physical and chemical technologies, e.g. membrane separation [24–26].

Titanium dioxide is the most studied photocatalyst and considered highly desirable because of its low cost, non-toxicity, low environmental impact, significant oxidizing power, outstanding photocatalytic activity, and long-term (photo)stability [27–29]. However, it presents some disadvantages. Because of large band energy, it can only be activated by UV light and the fast recombination rate of the photoexcited electron-hole pairs makes its use not very effective. To address this issue, different strategies can be pursued [29–32]. The treatment by ultrasound was effective in forming oxygen vacancies which allow activation under visible light [33,34]; the coupling of TiO_2 with other suitable semiconductor materials can improve the solar light absorption, enhance the photocatalytic activity and change the surface acidity [35–39]. Moreover, the doping with metals (i.e., Nb, Cu, Co, Ni, Au) has been reported to be effective

in the reduction of the recombination rate of photoexcited electron-hole pairs and modification of some surface features [26,39–45]. Cu_2O-based materials are used for a broad range of applications, such as sensing, disinfection, desulfurization, organic synthesis, photovoltaics, photodegradation, and photocatalysis. TiO_2 is a widely studied n-type semiconductor, whereas Cu_2O is a typical p-type semiconductor with a low band gap of 2.2 eV. They might come together to form a p-n heterojunction, which can absorb solar spectrum radiation, boost photogenerated charge carrier separation, and increase photocatalytic performances [46–49]. Notably, by considering the energetic level of Cu_2O conduction band edge, the hydrogen production can be boosted [36,50,51].

TiO_2 exists in three main crystalline phases, i.e. rutile, anatase and brookite that exhibit different photocatalytic activity [52–56]. Brookite, the relative new polymorph [52], has shown to be active towards the partial oxidation of glucose and towards the formation of hydrogen [57,58]. Platinum (Pt), on the other hand, was widely used in photo-reforming reactions due to its largest work function (5.65 eV), higher stability with respect to other metals and the lowest over potential for H_2 formation [33,58–60]. In recent years, the efforts of the scientific community have turned to the search for ecological and economic alternatives to noble metals and Cu_2O has received wide acclaim [36,61,62].

In this work, TiO_2-based photocatalysts (anatase, rutile and brookite) modified by Pt loading, Nb doping and coupled with Cu_2O were compared towards glucose and fructose reforming, used as probe molecules of biomass derivatives. Slightly different synthesis procedures were used to prepare the polymorphic forms of TiO_2. The surface and the chemical-physical properties of synthesized catalysts have been thoroughly studied with the aim of correlating the photoactivity to some features of the solids and highlight the role of Pt, that is worldwide used only as electrons sink. Notably, it was found that the noble metal had an important unusual role to modify the surface acid-base properties of the photocatalysts as indicated by the DRIFT and TPD characterizations.

Experimental

Chemicals

Ethanol (C_2H_5OH), titanium tetrachloride 98% ($TiCl_4$), hydrochloric acid 37% (HCl), titanium(IV) isopropoxide $\geq$ 97% ($Ti(OCH(CH_3)_2)_4$) named as TIP, Pluronic P127, copper(I) chloride (CuCl), niobium(V) chloride ($NbCl_5$), copper(I) oxide (Cu_2O) and platinum chloride ($PtCl_4$) were purchased from Sigma-Aldrich and used without further purification for the

synthesis of different photocatalysts. Commercial samples of BDH (anatase) and P25 (anatase + rutile) were also used as reference materials and for the purpose of comparison.

Catalysts preparation

Brookite

Brookite was prepared through hydrothermal hydrolysis. 210 mL of distilled water, 80 mL of HCl (concentrated) and 5 mL of $TiCl_4$ were added in a 500 mL beaker under stirring. After ca. 2 h the mixture was shifted into a Pyrex bottle and heated at 373 K in an oven for 48 h. The resulting combination powder was a mixture of brookite and rutile. By peptizing with water at different times, pure brookite nanoparticles were recovered in the supernatant and rutile phase was present as a precipitate. This sample was identified as Brookite.

Niobium (Nb) loading was accomplished by adding $NbCl_5$ to the solution obtained by dissolution of $TiCl_4$. Nb1-brookite was the code used for this sample where 1% indicates the nominal weight percentage of Nb with respect to TiO_2. Nb was chosen both because it enhances the photoactivity of TiO_2 [26,63] and because it modifies its surface acid properties [64].

Home prepared TiO_2 (HP)

The sample indicated as HP was prepared by adding titanium(IV) isopropoxide (TIP) to an aqueous solution containing HCl, Pluronic P127 and C_2H_5OH. The following molar ratios were used: TIP (1): H_2O (15): C_2H_5OH (40): HCl (0.5): P127 (0.005). The resulting dispersion was mixed for approximately 4 hours at room temperature and then heated overnight at 383 K. The recovered solid was calcined for 24 h at 773 K.

Cu_2O-TiO_2 samples

Some Cu_2O (3 wt%)-TiO_2 coupled samples were prepared by mixing the two oxides by a Retsch Ball Mills, type PM100 ball milling. The powders were mixed for 2 hours at 150 rpm, reversing the sense of the rotation after 1 hour and 10 minutes of pause. The Cu_2O percentage was chosen considering the results obtained in a previous paper [36].

Pt-loaded samples

Some TiO_2 catalysts were loaded with 0.5 wt% Pt by a photodeposition method. Distilled water (200 mL), ethanol (50 mL), $PtCl_4$ (5 mL) and TiO_2 based sample (1 g) were added in a

photoreactor. The obtained mixture was stirred in the dark for 0.5 h with He (or N_2) bubbling, and then illuminated with a UV lamp (125 W) for 7 h. The resulting mixture was filtered, washed thoroughly with distilled water and then dried in an oven for 6 h.

Catalysts characterization

X-ray diffraction (XRD) patterns of the investigated powders were obtained by a Philips diffractometer (operative at a current of 30 mA and a voltage of 40 kV) using the CuKα radiation. The morphology was examined by scanning electron microscopy (SEM) using a Nova NanoSEM instrument. A small amount of powder samples was placed on carbon tape attached to a stainless-steel stub.

Transmission electron microscopy (TEM) was performed using a Titan transmission electron microscope operating at 300 kV. The samples were prepared by suspending the powder in 2-propanol, treating with ultrasound, and finally depositing 3 μL of the suspension 2 consecutive times on a 400-mesh Au grid provided by Tedpella. The solvent was then evaporated at room temperature. ImageJ was used to evaluate the lattice d-spacing and the size of the nanoparticles. The specific surface areas (SSA) were determined in a Flow Sorb 2300 apparatus (Micromeritics) by using the single-point BET method.

Zeta potential measurements were performed using a Malvern Panalytical Zetasizer Ultra Red instrument equipped with a Malvern Multipurpose Titrator MPT-3. 25 mg of a photocatalyst was dispersed in 100 mL of ultrapure water and stirred for 30 minutes (400 rpm). 0.25 M and 0.025 M hydrochloric acid and 0.25 M sodium hydroxide were used to adjust the pH in the measurement range.

The UV-Vis diffuse reflectance spectra (DRS) were acquired in the wavelength range of 200-800 nm at room temperature by using a Shimadzu UV-2401 PC spectrophotometer with barium sulphate ($BaSO_4$) as the reference material. Band gap values were calculated by plotting the modified Kubelka-Munk function, $[F(R'_\infty)hv]^{1/2}$ against the energy of the stimulating light. The solid-state photoluminescence spectra (PL) of the investigated photocatalysts were recorded with a Perkin Elmer UV-Vis fluorescence spectrometer LS 55 in the range of 300-600 nm at an excitation wavelength of 300 nm. Raman spectra of the photocatalysts were obtained by means of a BWTek-i-micro Raman Plus System, equipped with a 785 nm diode laser.

X-ray photoelectron spectroscopy (XPS) was performed using a Thermo Fisher Scientific (TFS) Escalab Xi+ XPS with an AlKα X-ray source. Prior to the XPS measurements, the samples were etched *in situ* with an Ar beam to remove contaminants from the top layer.

For the identification of the free radical species of the catalyst, electron paramagnetic resonance (EPR) was performed on an EMX-nano spectrometer (Bruker Biospin Corp., Karlsruhe, Germany). For the detection of transition metals and oxygen vacancies, the powder was placed in a tube and was fitted into the sample holder in the EPR test chamber for analysis. For the detection of superoxide anion radicals ($O_2^{\bullet-}$), the sample was dissolved in methanol to form a 1 mg/mL suspension which was then dispersed using ultrasonication. Subsequently, 100 mM of trapping agent 5,5 Dimethyl-1-pyrroline N-oxide (DMPO) was added into the suspension. After stirring, the mixture was placed in a tube and was fitted into the sample holder in the EPR test chamber for analysis. For the detection of hydroxyl radical ($OH^{\bullet}$), the sample was dissolved in water to form a 1 mg/mL suspension which was then dispersed using ultrasonication. Subsequently, 100 mM of trapping agent 5,5 Dimethyl-1-pyrroline N-oxide (DMPO) and 100 µL of 1 mM H_2O_2 were added into the suspension. After stirring, the mixture was placed in a tube and was fitted into the sample holder in the EPR test chamber for analysis. The sample was irradiated for 30 minutes using a UV (LOT-Quantum Design GmbH) lamp and data were recorded.

The Diffuse Reflectance Infrared Fourier Transform Spectroscopy (DRIFTS) spectra of the studied catalysts after adsorption of pyridine were recorded using a Perkin Elmer Frontier FT-IR spectrometer equipped with a mercury cadmium telluride (MCT) detector. A catalyst sample placed in a DRIFTS cell was first heated in an N_2 stream from room temperature to 473 K and then held at this temperature for 15 minutes to remove impurities from the catalyst surface. The sample was then cooled to 393 K in an N_2 stream, and a background spectrum was recorded. After saturating the catalyst surface with a pyridine containing N_2 stream for 20 minutes at 393 K, the catalyst sample was purged with pure N_2 and held at 393 K for additional 2 hours to remove the excess pyridine. The FT-IR spectra (an average of 64 scans, resolution of 4 cm^{-1}) were recorded at 393 K.

Surface acidic sites were revealed using pyridine as a probe molecule and a Perkin Elmer Pyris 1 TGA instrument. Samples were first heated from 323 to 473 K and held at this temperature for 15 minutes to remove contaminants from the catalyst surface. The samples were then cooled to 393 K and pyridine was adsorbed with a saturated N_2 stream until the weight of the catalyst was constant (after about 20 minutes). The powders were then purged with N_2 and held at 393

K for 2 hours to remove excess pyridine. TPD (temperature-programmed desorption) profiles were recorded in the temperature range from 393 to 773 K.

To determine basic properties of the surface of investigated photocatalysts, CO_2 TPD profiles were obtained by heating samples in an O_2 (5%)/He stream (25 mL/min) from room temperature to 398 K (10 K/min) in the Micromeritics AutoChem II 2920 apparatus. After 10 minutes, the samples were cooled to 323 K and then the gas flow was changed to Ar (25 mL/min). CO_2 was introduced by dosing CO_2 (80 vol%)/Ar into the Ar stream (25 mL/min) flowing through the samples at 323 K. Desorption of CO_2 from the sample into the Ar stream (25 mL/min) was monitored over the temperature range of 323-633 K (heating ramp 10 K/min) using the Pfeiffer Vacuum ThermoStar mass spectrometer.

Photocatalytic activity determination

Photocatalytic activity was studied in anaerobic conditions by using separately two substrates, i.e. glucose and fructose, at room temperature and atmospheric pressure, monitoring the evolution of H_2 and CO_2 in the gas phase and the formation of the intermediates in the liquid phase. An 800 mL Pyrex cylindrical reactor was used, and He or N_2 were bubbled into the solution for 30 minutes to achieve the adsorption-desorption equilibrium of the substrate on the catalysts surface. After that, the reactor was sealed, and the near-UV lamp (125 W medium pressure Hg) was switched on. The initial concentration of the two substrates was 1 mM and the reactions were carried out at a pH of about 5, the "natural" pH of the aqueous suspension of both substrates measured after adding the catalyst. A radiometer was used to check the optimum amount of the photocatalysts able to absorb ca. 90% of the photons emitted by the lamp. Specific amounts ranging between 0.3 and 0.8 g/L were obtained for the different photocatalysts. To determine the substrates' adsorption on the catalyst surface in the absence of light, their concentration values were measured after 30 minutes of stirring of the suspension containing the catalyst under dark conditions. The experimental setup is shown in Figure S1. The photocatalytic reactions lasted 5 h and samples were withdrawn periodically during the irradiation time, and filtered by 2 µm membranes (HA, Millipore). A Thermo Scientific Dionex ultimate 3000 HPLC, equipped with a Diode Array and refractive index detectors, was used for the quantitative determination of glucose and fructose and for identifying their reaction products. The eluent was a 2.5 mM H_2SO_4 aqueous solution, the flow rate was 0.6 mL/min and the column was a Phenomenex REZEK ROA H^+ Organic acid H^+. In order to monitor the evolution of the gaseous species during the runs, 500 µL of the gas was drawn at specific time

intervals from a valve at the top of reactor. A HP 6890 Series GC System equipped with a Supelco packed column GC 60/80 Carboxen$^{TM-1000}$ and a thermal conductivity detector (TCD) was used to measure the content of H_2 and CO_2.

Results and discussion

Figure 1 shows the XRD patterns of all prepared photocatalysts. The three main polymorphs (anatase, rutile and brookite) of TiO_2 are indicated as A, R, B, respectively. The commercial TiO_2 BDH consists of only anatase phase, whereas P25 contains both the anatase and rutile phases. HP contains mainly anatase phase and also traces of rutile, pure brookite was home prepared. The commercial samples (P25 and BDH) show more intense and narrow peaks compared to those of the home prepared ones indicating a better crystallinity, due to their preparation at high-temperature on industrial scale. Moreover, no diffraction peaks related to foreign species are present, probably due to the high degree of the dispersion and the low amount of these species with respect to TiO_2.
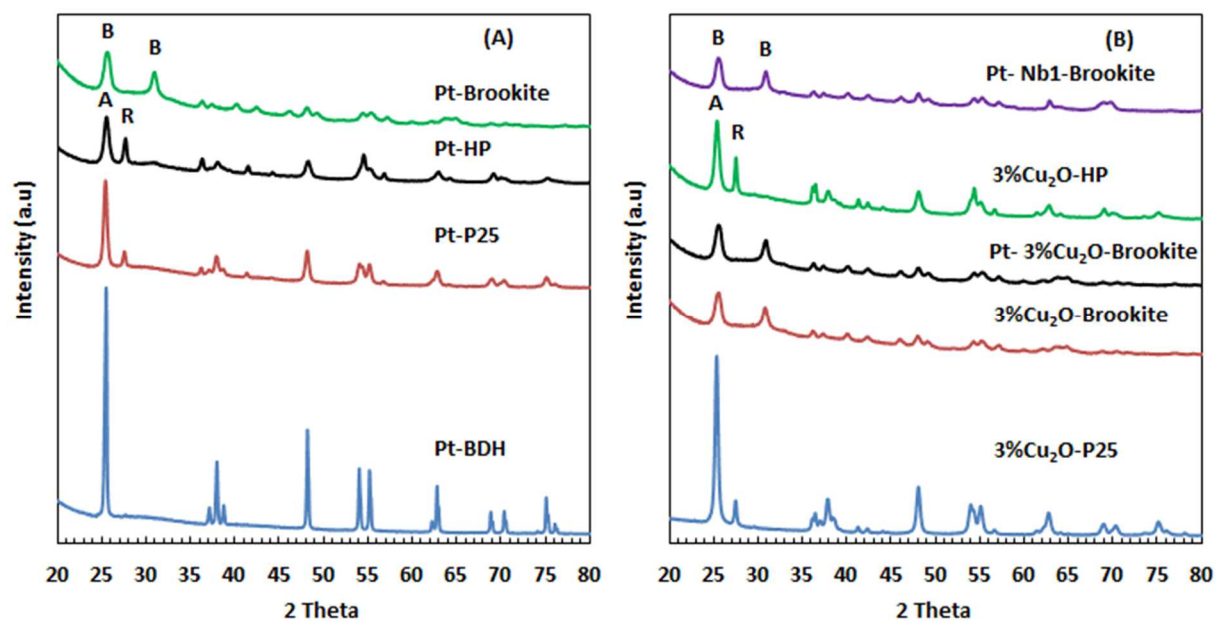
Figure 1. XRD patterns of: (A) Pt-BDH, Pt-P25, Pt-HP, and Pt-Brookite; (B) 3%Cu$_2$O-P25, 3%Cu$_2$O-Brookite, Pt-3% Cu$_2$O-Brookite, 3%Cu$_2$O-HP, and Pt-Nb1-Brookite samples. A = Anatase, B = Brookite, R = Rutile.

The crystal phase and specific surface area (SSA) of all the samples are listed in Table 1. Commercial samples exhibit lower SSA as compared to that of home prepared photocatalysts,

being 48 m^2·g^{-1} for 3%Cu$_2$O-P25 and 69 m^2·g^{-1} for 3%Cu$_2$O-HP, respectively. Brookite samples display higher SSA ranging between 90 and 98 m^2·g^{-1}, whilst Pt-BDH shows the lowest SSA of 10 m^2·g^{-1}.

SEM images of all prepared samples are displayed in Figure S2. All samples are formed by aggregates of irregular roundish particles whose size range is 30-130 nm. Due to the lower synthesis temperature, the particle sizes of homemade samples are smaller than those of commercial samples.

Diffuse reflectance spectra (DRS) of the different TiO$_2$-based samples are shown in Figure S3. All the photocatalysts absorb light in the UV–visible range. The BDH and Brookite samples (Figure S3A) show an absorption band in the high energy region ($\lambda < 360$ nm), whilst all other samples exhibit a slight shift in absorption towards longer wavelengths. Pt presence and copper loading (Figure S3B) enhance the absorption at $\lambda > 420$ nm and slightly shift the absorption edge towards the visible part of spectrum.

Band gap values of all samples, measured by plotting the modified Kubelka-Munk function, $[F(R'_{\infty})h\nu]^{1/2}$ against the energy of the stimulating light, are reported in Table 1. All the powders exhibit band gap values in the range of 2.96-3.33 eV being the lowest value found for HP and highest figures observed for brookite based samples. No relevant variation with respect to pristine TiO$_2$ samples were observed in the presence of foreign species.

Table 1. Some physical-chemical properties of the investigated photocatalysts: composition (A = Anatase, R = Rutile, B = Brookite), band-gap, SSA and TPD results (amount and density of acid sites of catalysts and the corresponding temperatures of pyridine desorption).

Catalyst	Phase	Band gap (eV)	SSA (m^2/g)	Quantity of acid sites (mmol/g)	Density of acid sites (mmol/m^2)	Temperature of pyridine desorption (°C)
BDH	A	3.24	10	0.0095	0.0010	289
Pt-BDH	A	3.26	10	0.0091	0.0009	[a]N.D.
P25	A+R	3.18	50	0.1194	0.0024	289
Pt-P25	A+R	3.09	50	0.0944	0.0019	323, 388
3%Cu$_2$O-P25	A+R	3.08	48	0.1253	0.0026	264, 342
Brookite	B	3.34	98	0.2721	0.0028	406
Pt-Brookite	B	3.32	98	0.4836	0.0049	235, 408

Pt-Nb1-Brookite	B	3.27	90	0.2669	0.0030	402
3%Cu$_2$O-Brookite	B	3.33	91	0.2237	0.0025	290, 413
Pt-3%Cu$_2$O-Brookite	B	3.33	94	0.2669	0.0028	290, 403
HP	A+R	2.96	78	0.1605	0.0021	310
Pt-HP	A+R	3.01	78	0.1137	0.0015	375
3%Cu$_2$O-HP	A+R	3.05	69	0.1537	0.0022	261, 350
Cu$_2$O	Cu$_2$O	1.97	1	0.0009	0.0009	428

[a]N.D.: Not determined because no pyridine desorption peak was observed in the measured temperature range (see Figure S8).

Figure S4 shows the Raman spectra of TiO$_2$ based composites. Raman bands at 144 cm^{-1} (E$_g$), 197 cm^{-1} (E$_g$), 396 cm^{-1} (B$_{1g}$), 514 cm^{-1} (A$_{1g}$), and 637 cm^{-1} (B$_{1g}$) are characteristic of anatase phase, whilst those at 446 cm^{-1} and 613 cm^{-1} are related to the rutile one. In P25 and HP based samples, being anatase the main component, the presence of rutile can be detected by enlarging the figures while there are no peaks relating to Cu$_2$O due to probably its small amount and dispersion within the TiO$_2$ matrix. In Figure S4B the bands at 126 cm^{-1}, 152 cm^{-1}, 212 cm^{-1}, 247 cm^{-1}, 322 cm^{-1}, 364 cm^{-1}, 409 cm^{-1}, 456 cm^{-1}, 498 cm^{-1}, 543 cm^{-1}, 582 cm^{-1} and 632 cm^{-1} are characteristic of brookite. In brookite-containing samples, the addition of the metal caused a decrease of the band intensity that can be attributed to the greater surface disorder due to the presence of Pt on the TiO$_2$ surface. There were no identifiable peaks of Pt, and this is consistent with the observation that this metal is not present within the TiO$_2$ lattice but only on the surface. Also in this case no Cu$_2$O peaks were detectable.

Figure 2 displays the zeta potential versus pH curves of some Pt-TiO$_2$ samples. The IEP (isoelectric point, i.e. the pH value at which the net charge on the catalyst surface is zero) values are 4.23 for Pt-BDH, 4.45 for Pt-HP, 5.00 for Pt-P25 and 5.63 for Pt-Brookite. The above findings imply that at pH 5 (pH at which the photocatalytic runs were carried out) the catalyst's surface is negatively charged for Pt-BDH and Pt-HP, neutral for Pt-P25 and positively charged for Pt-Brookite. Then different coulombic interactions can take place between the species in the reaction mixture and the surface of the various TiO$_2$ powders [65].
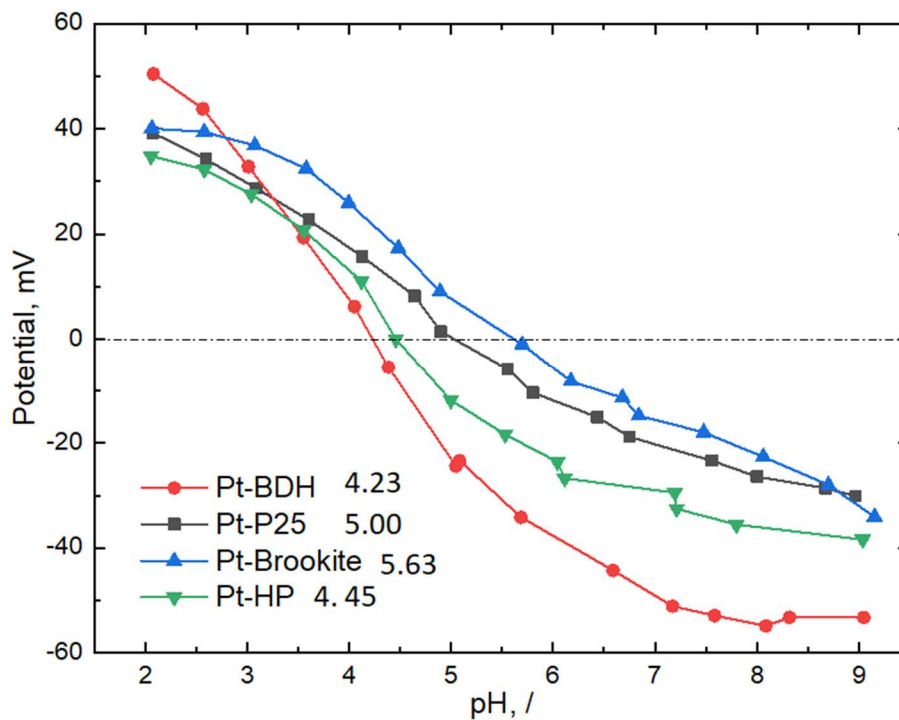
Figure 2. Results of the pH-related zeta potential measurements.

The presence of noble metals such as Pt has been reported to be effective for the visible-light activation and the enhancement of the TiO_2 performance [66]. In fact, the Fermi levels of noble metals are lower than that of TiO_2, and this results in the transfer of the photogenerated electrons from the conduction band of TiO_2 to metal particles [67]. This process reduces the electron–hole recombination rate as can be seen from the decrease of the intensity of the photoluminescence bands in the presence of Pt (Figure 3) [68]. For all the samples, except for BDH which displays a peak at 380 nm, the main emission bands are at ca. 423 nm and this can be attributed to the band-to-band indirect transition of electrons in TiO_2 in accordance with the band gap values. The signals at higher wavelength can be assigned to a non-radiative recombination of the excited electrons towards lattice defects [51,69]. A significant decrease in the PL intensity can be noticed after the coupling with Cu_2O and the addition of Nb due to the lower recombination rate of the photogenerated charges [36].
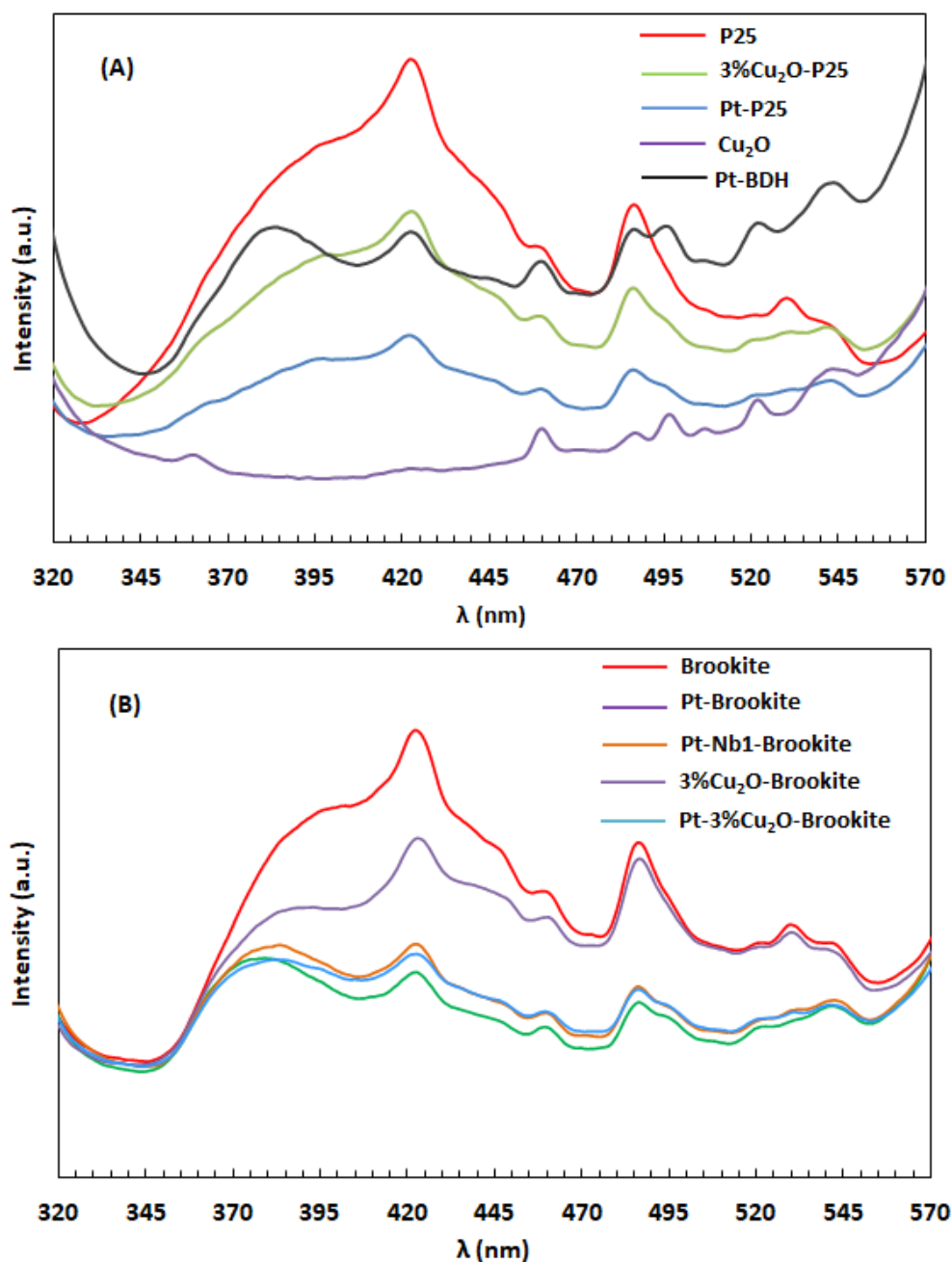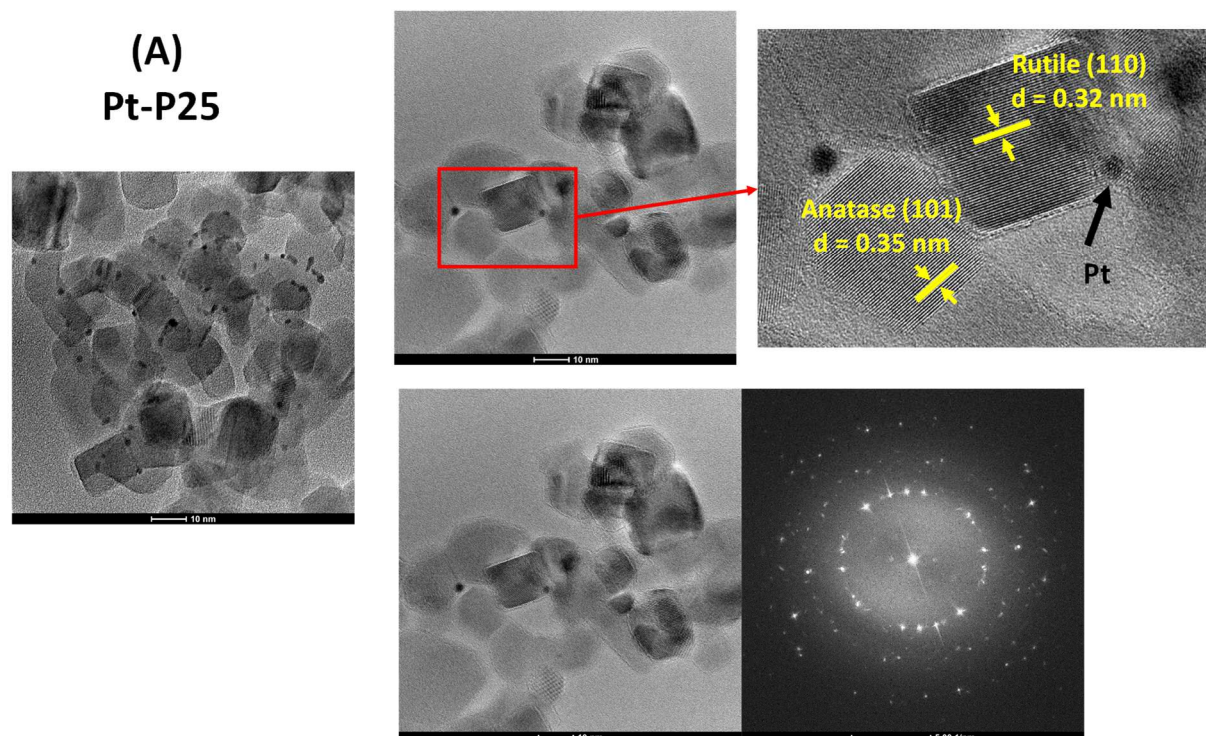
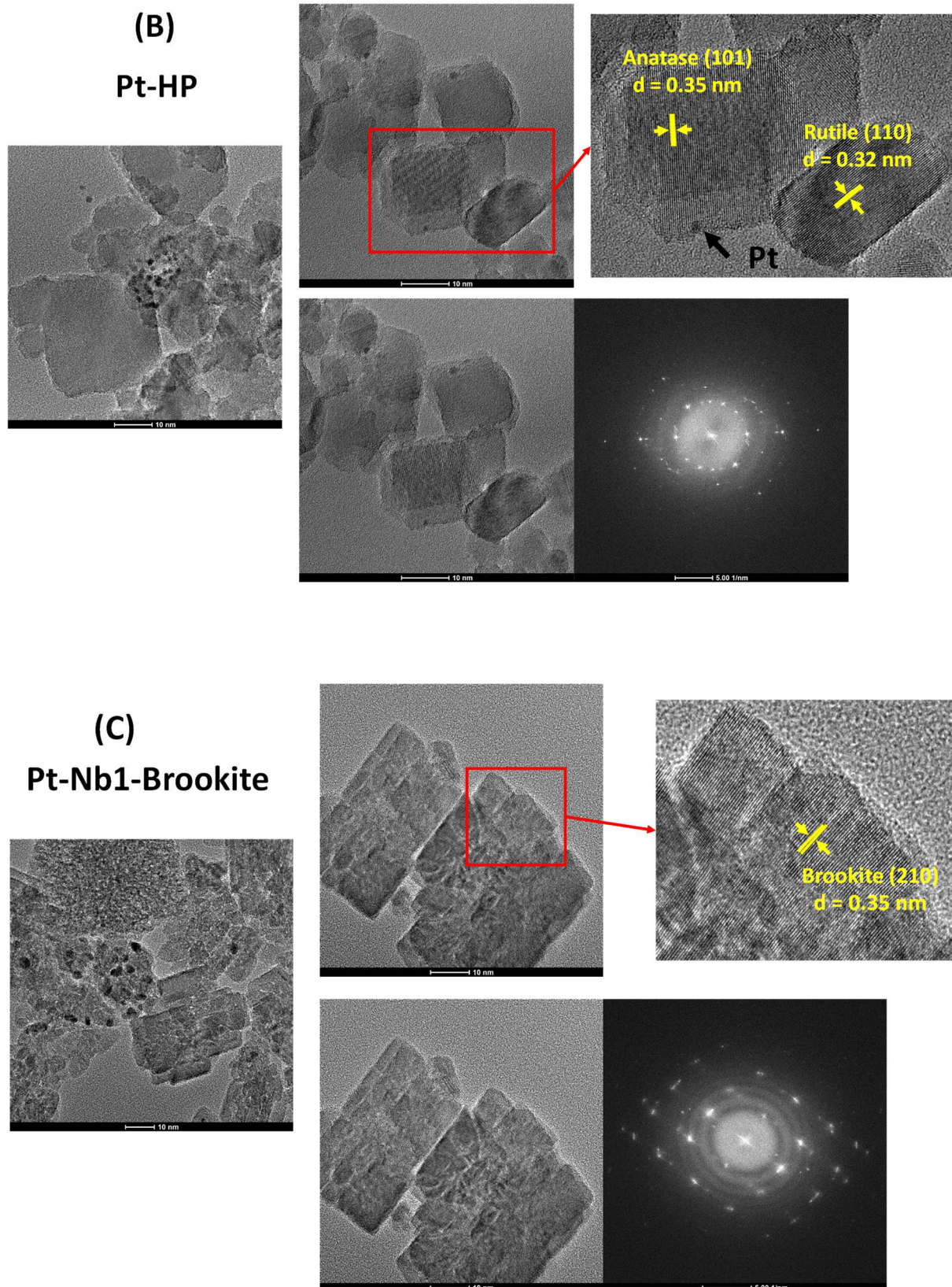**Figure 3.** Photoluminescence spectra of the different samples.

TEM images of the different samples were acquired to investigate the morphology, the particles dimension, and the distribution of the different components. Some selected images are reported in Figure 4, images of other samples are given in the Supporting Information (Figure S5). TEM images of the sample Pt-P25 (Figure 4A) reveal that Pt nanoparticles (represented by small dark spheres) are uniformly dispersed across the P25 surface confirming the effectiveness of the photodeposition method. The size of Pt nanoparticles is approximately 2 to 3 nm while the size of P25 particles (anatase and rutile) ranges between 10 to 20 nm. By zooming in on the image,

it is possible to distinguish two lattice fringes of ca. 0.35 nm and 0.32 nm, characteristic of the (1 0 1) anatase and (1 1 0) rutile planes, respectively [70]. SAED (selected-area electron diffraction) patterns consisting of concentric rings indexed as the various planes of rutile and anatase, confirmed the biphasic structure of P25. In the HP sample (Figure 4B), instead, Pt nanoparticles are clustered into one area on the TiO_2 surface. The size of TiO_2 particles ranges between 5 to 25 nm, which is slightly larger range compared to the Pt-P25 sample, and the size of Pt nanoparticles is ca. 1 to 2 nm that is slightly smaller than found in the Pt-P25 sample. Also, in this case an intimate contact between anatase and rutile can be observed.

Brookite consists of rod-shaped particles which size ranges between 10 to 30 nm (Figure 4C). Pt nanoparticles (dimensions ca. 2-3 nm) are concentrated in some areas whilst Nb particles are not distinguishable due to their low quantity and high degree of dispersion in the TiO_2 matrix. In the Cu_2O/TiO_2 composite samples a good contact between the two components can be clearly seen in the images reported in Figure S5. The sizes of Cu_2O particles range between 5 to 10 nm, which are smaller than those of TiO_2 particles.

(B)

Pt-HP

Anatase (101)
d = 0.35 nm

Rutile (110)
d = 0.32 nm

Pt

(C)

Pt-Nb1-Brookite
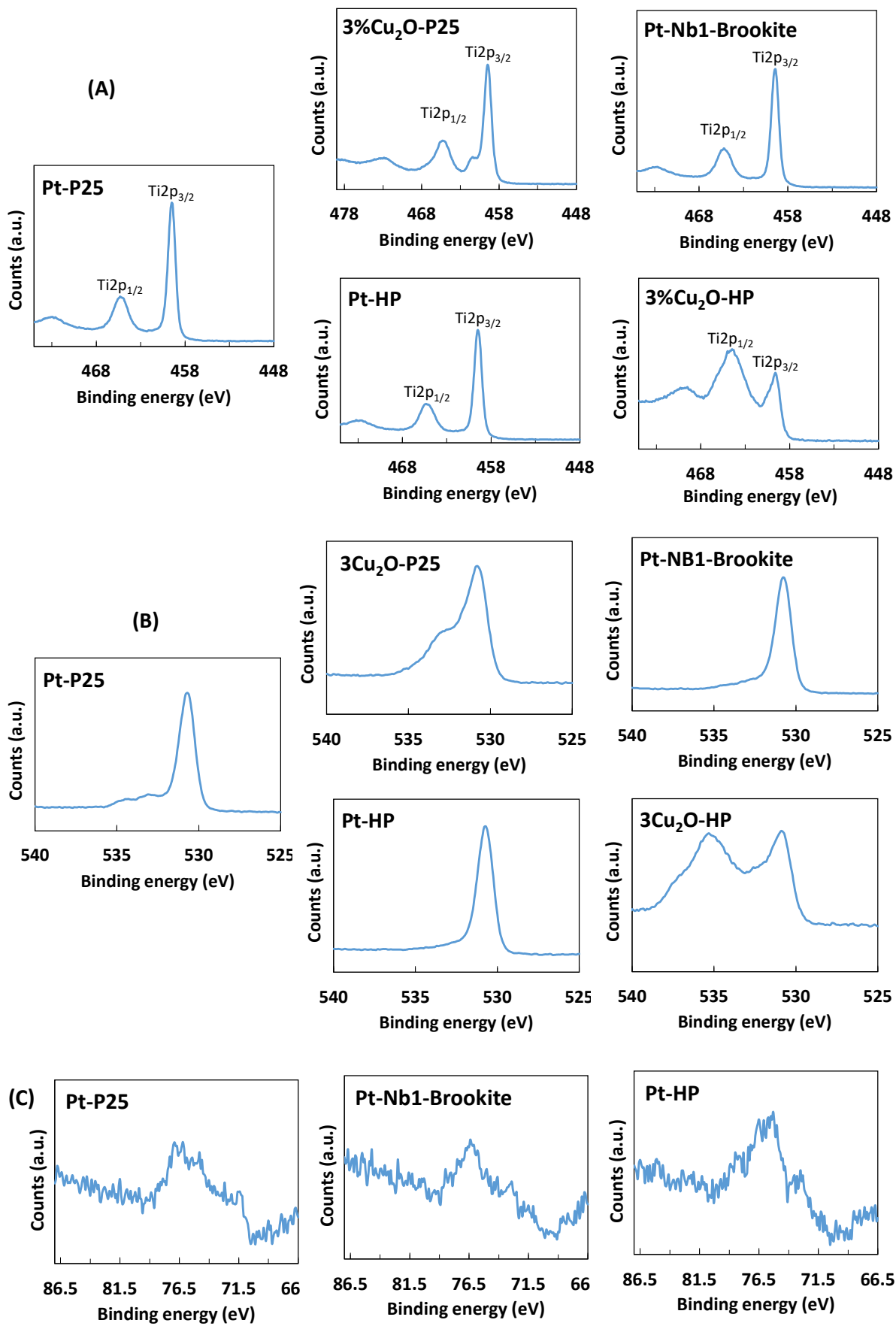
Brookite (210)
d = 0.35 nm

Figure 4. TEM images of the samples: (A) Pt-P25, (B) Pt-HP, and (C) Pt-NB1-Brookite.
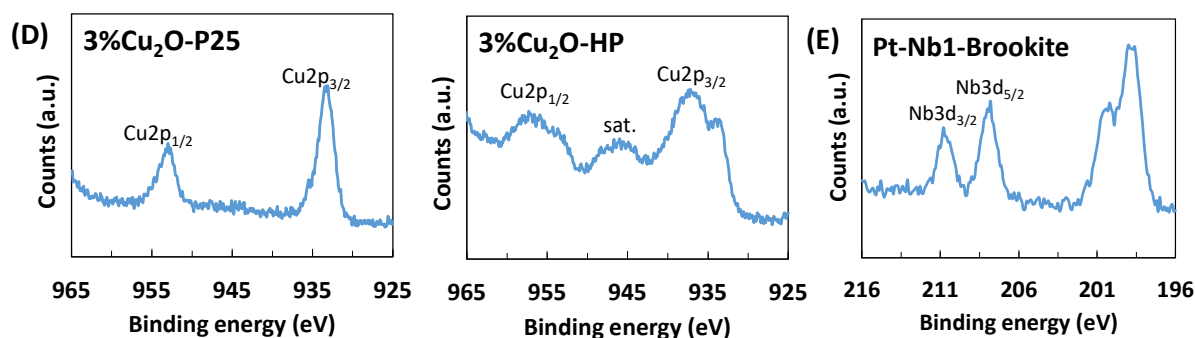
XPS measurements of some selected samples were carried out to examine the surface composition and the oxidation states of the different species. In Figure S6 the XPS survey spectrum of the samples with the various species indicated is presented. Peaks for Pt (not shown in XPS survey) were barely detected due to its small atomic concentration. Cl, as residual species deriving from $TiCl_4$, $PtCl_4$ and $NbCl_5$ precursors, was also detected. When both present, Cl and Nb are not clearly distinguishable because their peaks almost overlap. In Figure 5A are reported the high resolution XPS spectra of the Ti 2p peaks. In Pt-P25 sample the two peaks of Ti $2p_{3/2}$ at 459.5 eV and Ti $2p_{1/2}$ at 465.3 eV with a binding energy distance of 5.8 eV are characteristic of Ti^{4+} in TiO_2 [71]. The Ti $2p_{3/2}$ shoulder peak at 461.4 eV which is visible only for the 3%Cu_2O-P25 sample is characteristic of Ti^{3+}. This indicates that in this sample Ti is present in two oxidation states (+3 and +4) due to an electron transfer from Cu_2O to P25. The high-resolution O 1s spectra are shown in Figure 5B. For almost all of the samples the main peak is that at ca. 530.7 eV, assigned to O^{2-} ions of the TiO_2 crystalline lattice. The peak at ca. 533.0 eV, related to -OH groups [72], is negligible in Pt-Nb1-Brookite, small in Pt-P25, more evident in 3%Cu_2O-P25 and comparable to that at higher energy for 3%Cu_2O-HP. The presence of Cu_2O seems to favour the formation of surface hydroxyl groups. The main Pt peak at ca. 76 eV (Figure 5C) corresponds to Pt^0, the less intense peaks at lower binding energy are characteristic of partially oxidized Pt species [73].

High resolution XPS spectra of Cu 2p are reported in Figure 5D. For the P25 sample, the binding energy of the Cu $2p_{3/2}$ peak at 955.4 eV and of $2p_{1/2}$ at 933.2 eV are characteristic of Cu(I) oxide. For the HP sample the presence of a shakeup satellite peak between the main two Cu 2p peaks is characteristic of Cu^{2+} ions. The Nb 3d spectrum (Figure 5E) displays two peaks at 209.9 eV and 207.1 eV (binding energy distance of 2.8 eV) characteristic of Nb_2O_5 [74]. The other two peaks at lower binding energies are those of Cl 2p.

In Table S1 the atomic concentrations of the different species obtained by XPS investigations are reported.

(A)

Pt-P25

3%Cu₂O-P25

Pt-Nb1-Brookite

Pt-HP

3%Cu₂O-HP

(B)

Pt-P25

3Cu₂O-P25

Pt-NB1-Brookite

Pt-HP

3Cu₂O-HP

(C)

Pt-P25

Pt-Nb1-Brookite

Pt-HP

Figure 5. High resolution XPS spectra of: (A) Ti 2p, (B) O 1s, (C) Pt 4f, (D) Cu 2p, and (E) Nb 3d.

As illustrated in Figure S7, the EPR spectra of the powder samples 3%Cu$_2$O-P25, 3%Cu$_2$O-HP and Pt-3%Cu$_2$O-Brookite show a broad signal at g = 1.999 which can be assigned to Ti^{3+} ions on the surface [75]. The experiments carried out with samples containing Nb did not show any EPR signal, pointing out that the photocatalysts are unable to generate free electrons and oxygen vacancies under illumination. The Pt-3%Cu$_2$O-Brookite sample shows the highest intensity peaks indicating stronger presence of free electrons and oxygen vacancies, probably because the electrons are transferred to Pt and trapped therein. Conversely, the 3%Cu$_2$O-P25 solid showed the lowest EPR peak intensity. In the presence of DMPO/MeOH solutions (Figure 6), the experiments carried out in the dark cannot detect any EPR signal, indicating that the photocatalysts are unable to generate radicals in absence of illumination. When the photocatalysts get exposed to light, the EPR spectra give rise to the characteristic paramagnetic resonance absorption of the adducts of DMPO-•O$_2^-$. This result indicates that all the photocatalysts can thermodynamically produce superoxide anion radicals (•O$_2^-$) under illumination.

17
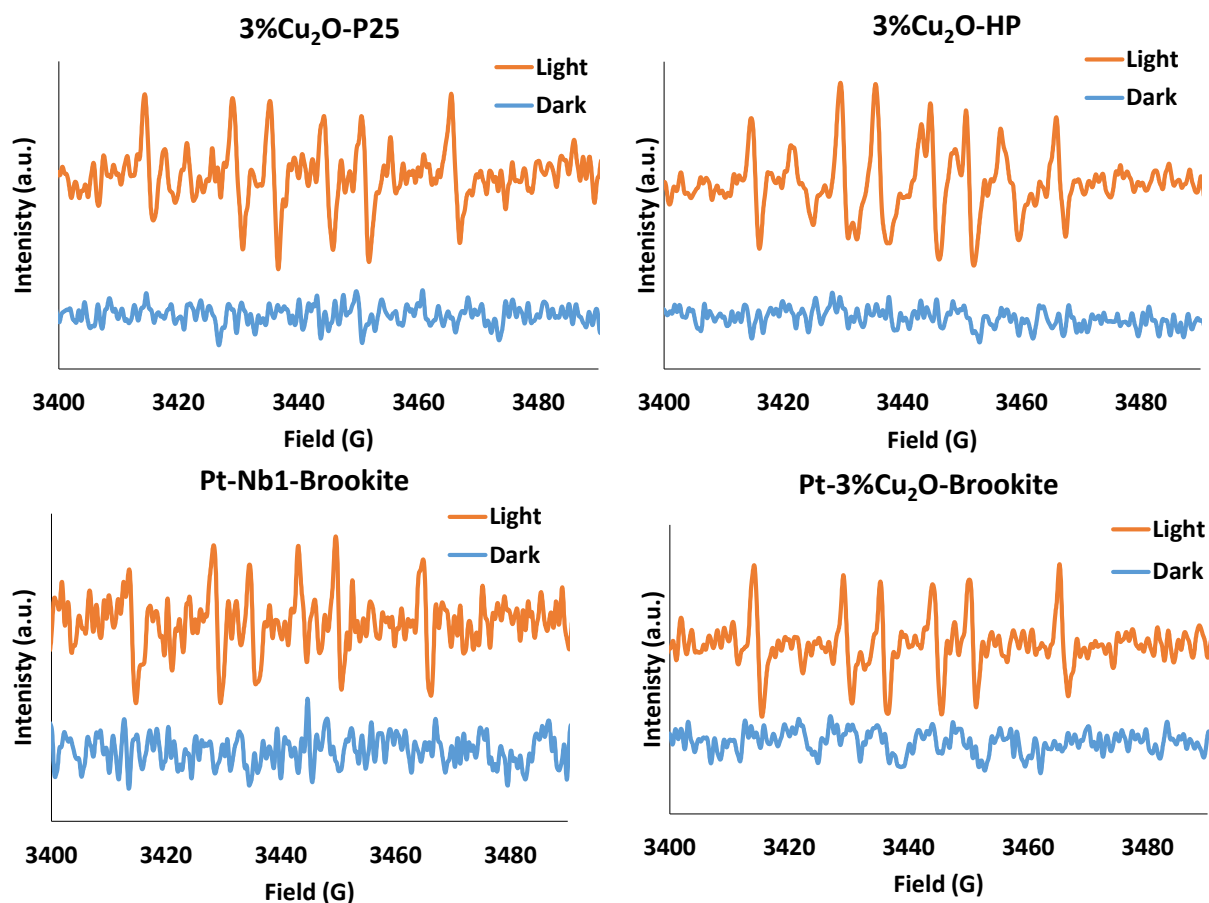
**Figure 6.** EPR spectra of MeOH suspended samples in the presence of DMPO.

For DMPO/H_2O_2/water suspended samples (Figure 7), in the dark, no EPR signal is detected. Under irradiation, the EPR spectra give rise to the characteristic paramagnetic resonance absorption of the adducts of DMPO-•OH. Results indicate that only 3%Cu_2O-P25 and 3%Cu_2O-HP samples can thermodynamically produce hydroxyl (•OH) radicals under illumination. Samples with brookite phase TiO_2 were unable to produce •OH radicals under light. While brookite TiO_2 can still exhibit some photocatalytic activity, it's often less efficient in generating hydroxyl radicals under light compared to anatase and rutile. This is due to the variations in electronic structure, band gap, and surface properties among the different TiO_2 phases. The P25 sample showed the highest intensity peaks indicating strongest formation of the hydroxyl radicals.
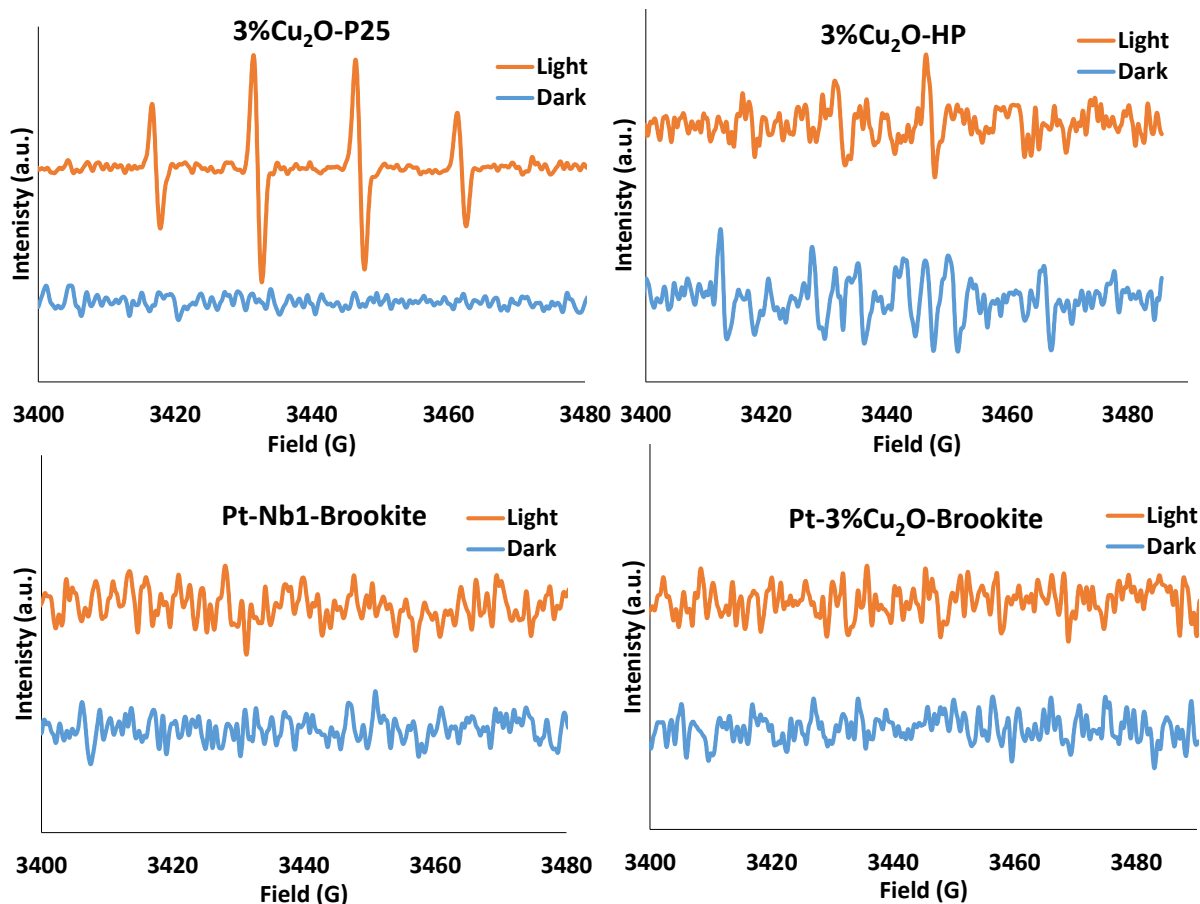
Figure 7. EPR spectra of water suspended samples in the presence of DMPO and H_2O_2.

In situ DRIFTS of adsorbed pyridine was used to identify the nature and the density of surface acid sites. In Figure 8 are illustrated the spectra related to bare and different Pt-loaded TiO_2 samples. The peaks at 1445 cm^{-1}, 1486 cm^{-1}, 1574 cm^{-1} and 1604 cm^{-1} are related to the pyridine ring coordinated to surface Lewis acid sites, whilst those at 1545 cm^{-1} and 1635 cm^{-1} correspond to the Brønsted acid sites on which the pyridinium ions are adsorbed [76–80]. A clear predominance of acidic Lewis sites is detectable in all samples; in addition, these spectra show the presence of both protonated pyridine (1545 and 1635 cm^{-1}) and co-ordinated pyridine (at 1604 and 1445 cm^{-1}). The peak at 1574 cm^{-1} is ascribable to a weak interaction of pyridine with the acid sites on the catalyst surface. Sharp and intense peaks are present for commercial P25 and home prepared HP samples, moderate for brookite and very weak for BDH solids. Although these spectra essentially give qualitative information, we can roughly say that a higher intensity corresponds to a higher concentration of acid sites, consequently the BDH sample exhibits the lowest concentration of surface acid sites, while P25 and HP solids the largest. Pt loading causes a decrease in the intensity of the bands for P25 (Figure 8A) and HP (Figure 8C) samples, a little

19

increase for BDH solid (Figure 8B) and a significant rise for Brookite sample (Figure 8D). The different effects of Pt on the various samples can probably be due to the diverse TiO$_2$ phases. Shifts to higher wavenumbers of the peaks at 1604 and 1445 cm^{-1} observed in Figures 8B and 8D for the spectra of Pt-BDH and Pt-Brookite samples could be due to electronic effects of Pt ensembles on the pyridine ring coordinated to Lewis acid sites on the surface.
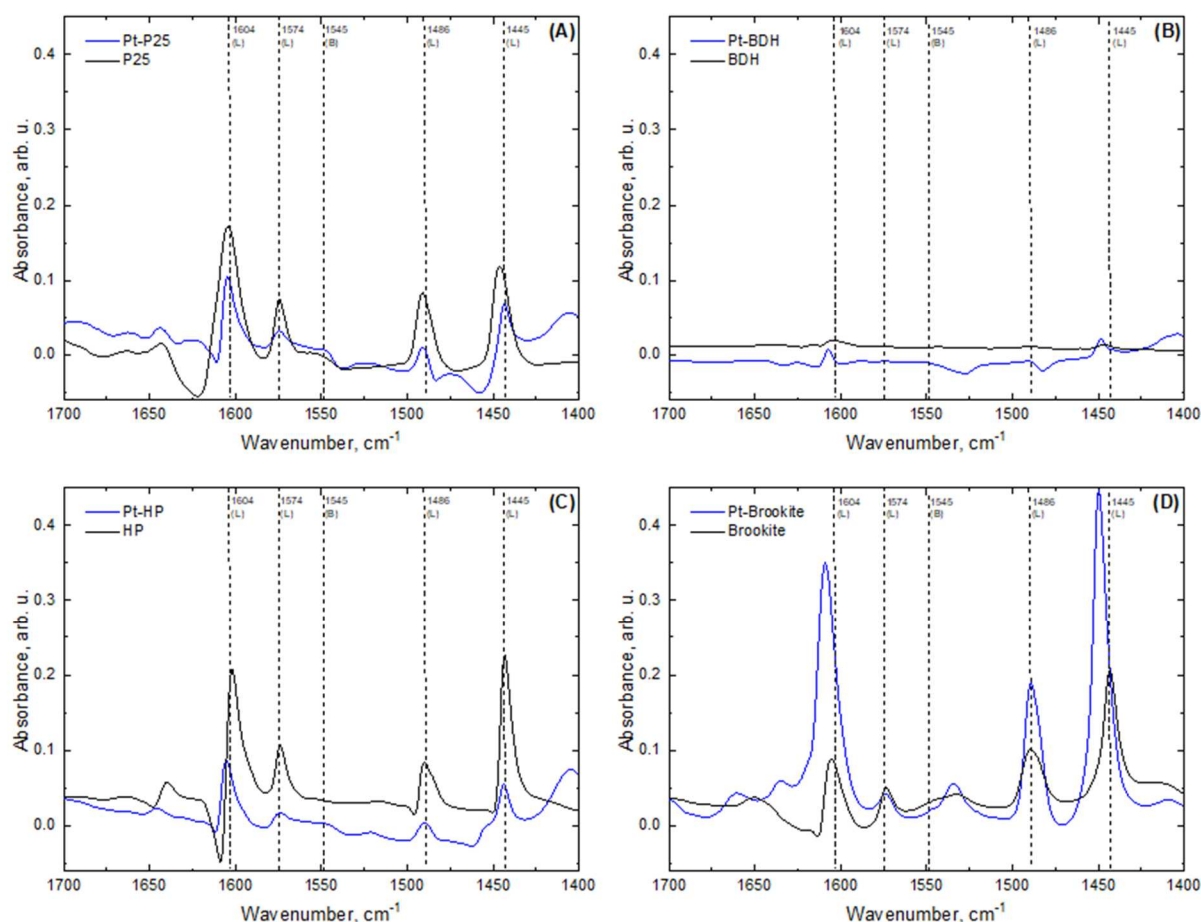
Figure 8. DRIFTS spectra of pyridine adsorbed on the surface of investigated materials; (A) P25 based solids, (B) BDH based samples, (C) HP based materials, and (D) brookite based photocatalysts.

In Table 1 are also reported the quantitative results related to pyridine TPD measurements in terms of amount and density of acid sites present on the surface of different catalysts, and the corresponding temperatures of pyridine desorption. Pyridine TPD profiles are shown in Figure S8. Comparing the pristine TiO$_2$ samples, Brookite and BDH solids display the highest and the lowest amount of acid sites, respectively; P25 sample shows less than half with respect to Brookite sample and HP solid has an intermediate amount. After Pt deposition one can notice a decrease of the quantity of acid sites in all the TiO$_2$ bare samples, except for Brookite solid, and the appearance of a second desorption peak except for HP sample. Moreover, a general increase

in the temperature of pyridine desorption can be observed in the presence of Pt, which implies a rise in the acid strength of the sites. The coupling with Cu_2O commonly reduces the desorption temperature and has different effects on the quantity of acid sites present on the various samples. In particular, it has a little effect on the amount of acid sites in P25 and HP samples, whilst a decrease is observed in Brookite solid. The latter is the only sample in which, in the presence of Cu_2O, the desorption temperature of the pyridine is practically equal to that of the bare sample. Moreover, a second desorption peak at higher temperature is visible. In the Pt-Nb1-Brookite sample, the addition of Nb reduces the amount of acid sites with respect to Pt-Brookite sample and has not influence on the temperature of pyridine desorption.

The TPD technique after CO_2 adsorption on TiO_2 surface allows to study the basic surface properties of the different catalysts. In Figure 9 are shown the CO_2-TPD profiles of the investigated samples and in Table 2 are reported the amounts of basic sites. The peaks between 323-423 K are ascribed to the desorption of molecular CO_2, whilst those at higher temperatures to HCO_3^- or carboxylate deriving from the interaction of CO_2 with the TiO_2 surface hydroxyl groups [81]. The presence of peaks at higher temperatures indicates the existence of a stronger adsorption of CO_2 on the catalysts.

The observation of Table 2 related to pristine TiO_2 reveals that pure anatase (BDH sample) exhibits the least number of basic sites, the mixtures of anatase and rutile (P25 and HP solids) have the same middle amount, whilst brookite possesses the highest quantity. After the Pt addition, an increase, except for BDH sample, can be noted and Pt-P25 solid displays the largest amount of basic sites in the high temperature range.
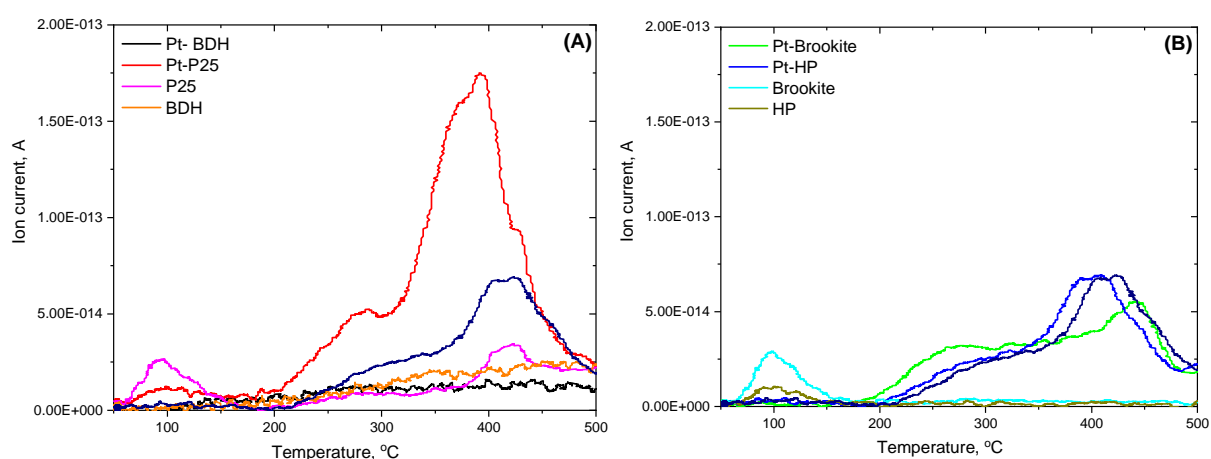
Figure 9. CO_2 TPD profiles of investigated materials.

Table 2. Amount and density of basic sites on the surface of investigated materials determined by TPD in the presence of CO_2.
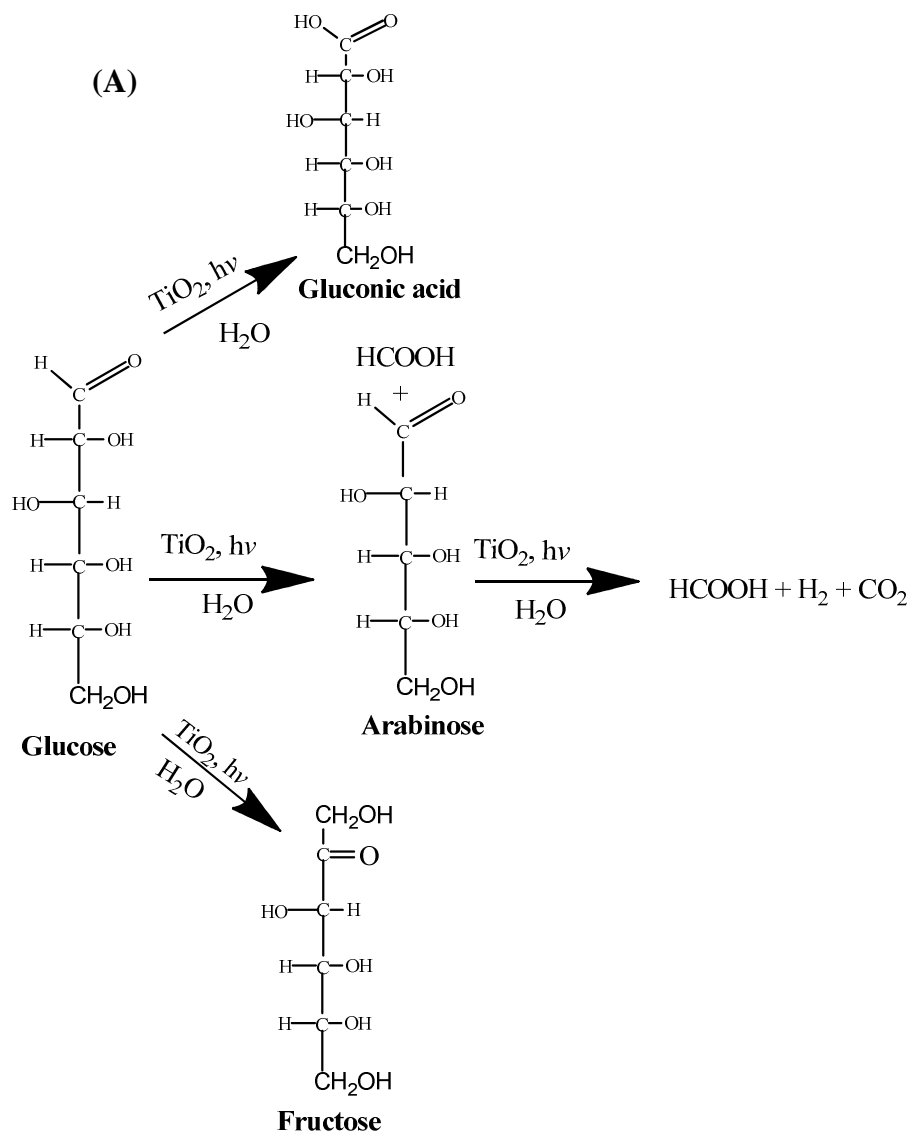
Sample	Mass of catalyst (g)	Peak area (A s)	Amount of basic sites (µmol/g)	Density of basic sites (µmol/m^2)
BDH	0.0447	2.95 E^{-11}	8.14	0.814
Pt-BDH	0.0521	2.09 E^{-11}	8.05	0.805
P25	0.0507	3.688 E^{-11}	12.1	0.242
Pt-P25	0.0518	1.287 E^{-10}	81.7	1.634
Brookite	0.0518	1.85 E^{-11}	28.3	0.288
Pt-Brookite	0.0502	5.75 E^{-11}	74.7	0.762
HP	0.0499	7.38 E^{-12}	12.8	0.164
Pt-HP	0.0520	5.74 E^{-11}	53.6	0.687

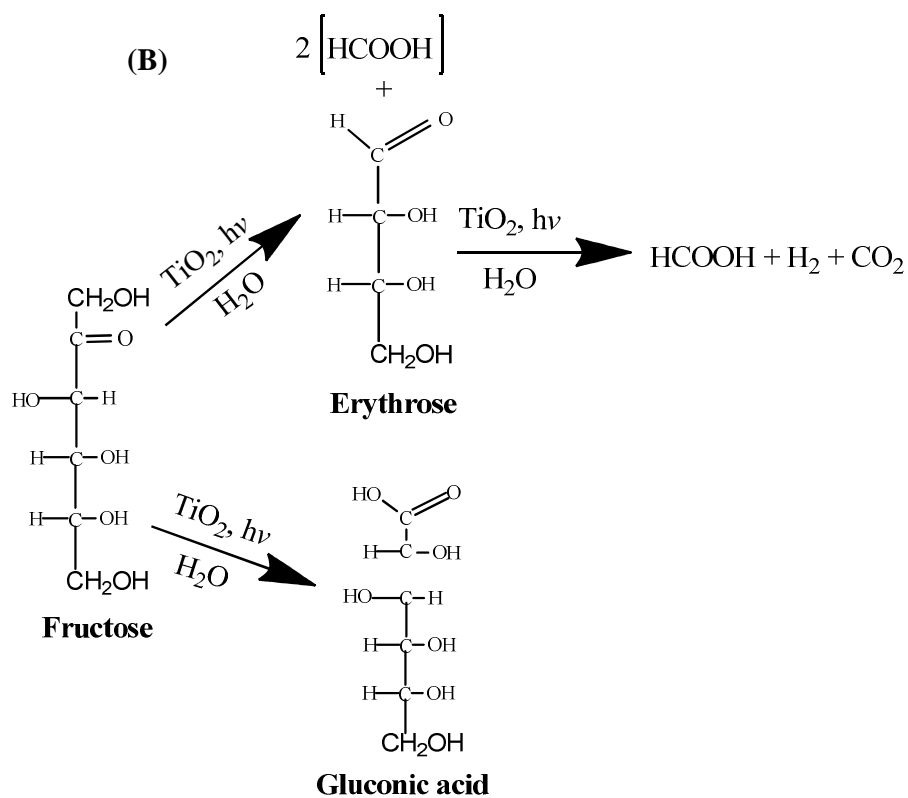## Photocatalytic conversion of glucose and fructose

All TiO_2 based samples were compared for glucose and fructose aqueous photo-reforming under UV light irradiation in anaerobic conditions with the aim to link the reactivity to some catalyst's features. The photocatalytic results obtained with the two substrates are reported in Tables 3 and 4. Pt enhances the photoactivity thanks to its role in the reduction of the recombination rate (in accordance with the PL results) and it is essential for H_2 production, as only compounds deriving from the partial oxidation of the starting substrates and CO_2 originating from mineralization were observed in the presence of naked TiO_2 [58]. The main identified intermediates in the liquid phase deriving from the partial oxidation of the starting substrates are arabinose, erythrose, gluconic acid, glucaric acid, fructose (starting from glucose) and formic acid (Scheme 1), whereas H_2 and CO_2 are measured in the gaseous phase present in the head space of the photoreactor. In Figure 10 are reported the concentration of glucose, fructose, the molecules obtained from their oxidation in liquid phase and those in the head space, CO_2 and H_2, versus irradiation time in the presence of the most active photocatalysts. All the samples give rise to the same compounds highlighting the same reaction mechanism (Scheme 1), but a different conversion degree, distribution of intermediates and H_2 production were observed with the different photocatalysts for both the substrates (Tables 3 and 4). The electronic and physico-chemical features of the different TiO_2 based materials, such as

recombination rate of the photogenerated charges, polymorphic form, hydroxylation degree, crystallinity percentages, surface interactions between the catalysts and the substrates, surface acidity, are the causes of their different photocatalytic behaviours [26,58,82].

Starting from glucose as substrate, fructose is formed by isomerization, and both can form gluconic acid by the oxidation of the anomeric C_1 center converting the aldehydic group to the carboxylic one. All the catalysts give rise to low amounts of glucaric acid starting both from glucose and fructose. A parallel mechanism consists in the α-scission of the carbohydrates giving rise to arabinose in the first step and erythrose in the second one along to formic acid and hydrogen [58,83,84]. In our experiment, starting from glucose, arabinose is the main product and traces of erythrose are observed with some catalysts, whilst starting from fructose, erythrose is essentially formed, confirming the breaking of the chain at the carbon bonded to carbonyl.

(A)

HO—C=O
|
H—C—OH
|
HO—C—H
|
H—C—OH
|
H—C—OH
|
CH₂OH
Gluconic acid

TiO₂, hv / H₂O →

H—C=O
|
H—C—OH
|
HO—C—H
|
H—C—OH
|
H—C—OH
|
CH₂OH
Glucose

TiO₂, hv / H₂O →

HCOOH
+
H—C=O
|
HO—C—H
|
H—C—OH
|
H—C—OH
|
CH₂OH
Arabinose

TiO₂, hv / H₂O → $HCOOH + H_2 + CO_2$

TiO₂, hv / H₂O →

CH₂OH
|
C=O
|
HO—C—H
|
H—C—OH
|
H—C—OH
|
CH₂OH
Fructose

(B)

$$2\left[HCOOH\right]$$

Fructose $\xrightarrow{\text{TiO}_2,\ h\nu,\ H_2O}$ Erythrose $\xrightarrow[\text{H}_2\text{O}]{\text{TiO}_2,\ h\nu}$ $HCOOH + H_2 + CO_2$

Fructose $\xrightarrow{\text{TiO}_2,\ h\nu,\ H_2O}$ Gluconic acid

Scheme 1. Hypothesized reaction mechanism of photo-reforming of (A) glucose and (B) fructose.
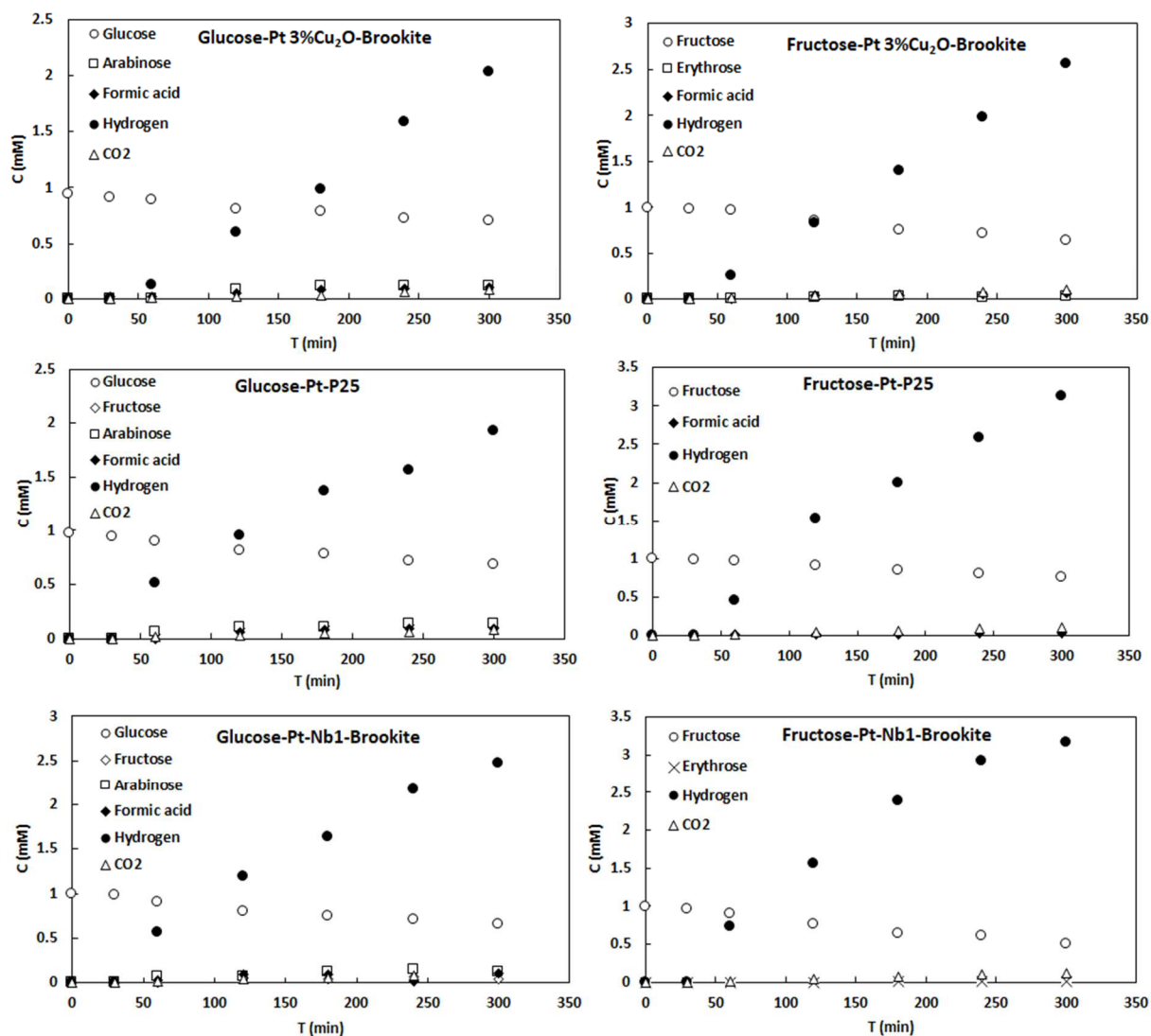
Figure 10. Concentration of (○) glucose, (◊) fructose, (□) arabinose, (x) erythrose, (♦) formic acid, (●) H_2, and (Δ) CO_2 versus irradiation time in the presence of various photocatalysts after 5 h of irradiation.

Negligible amounts of H_2 are formed by using the pristine TiO_2 samples and the largely used Pt was essential to obtain satisfactory amounts. The coupling of TiO_2 with Cu_2O is beneficial both for conversion and selectivity for P25 sample, whilst it exhibits a slightly negative effect on Brookite and HP solids, in any cases was effective in replacing Pt for H_2 formation, avoiding the use of noble metal species.

Home prepared samples were competitive with the commercial ones being more active than the benchmark P25 solid. The commercial samples afford less photocatalytic conversion for glucose and fructose than the home prepared ones. The highest glucose conversion (40%) is obtained with Pt-HP samples, whilst the most oxidant sample for fructose is Pt-Nb1-Brookite (conversion 50%). With the sample Pt-HP, almost the same degree of conversion is reached

with the two substrates, while for fructose lower selectivity values but greater quantities of H_2 compared to glucose are obtained.

With glucose Pt-Brookite based samples show a little increase in the conversion, a generally decrease in the fructose selectivity and an enhanced H_2 formation. By using Pt-Brookite and Pt-Nb1-Brookite samples, the conversion of glucose is similar, the Nb addition enhances H_2 formation and the selectivity towards the intermediates and fructose is also formed. HP based powders exhibit the highest conversion percentages and arabinose selectivity. The maximum hydrogen concentration is obtained with the Pt-Brookite photocatalyst that displays the highest amount of acidic cites. Among the Pt-containing samples, Pt-BDH solid exhibits the lowest glucose conversion and formic acid selectivity, the highest fructose selectivity and no arabinose formation indicating a different reaction pathway [58,84]. This finding is different from the results of Román-Leshkov et al. [85] who attributed the isomerization of glucose to fructose by using tin-containing zeolite Sn-Beta as catalyst to the presence of Lewis acidic sites. In our case the solid with the lowest number of acidic sites (Table 1 and DRIFT measurements) gives rise to the highest fructose formation. Probably other features as catalyst type (we use TiO_2 instead of zeolite-based catalyst) and preparation method play a fundamental role.

By using fructose as substrate, a lower selectivity towards the partial oxidation compounds is obtained with respect to glucose. The most efficient catalysts are Pt-Brookite and Pt-Nb1-Brookite both for conversion and production of H_2.

The obtained results highlight the peculiar role of the interactions between the substrates and the surface of a specific photocatalyst [26].

Table 3. Glucose conversion, selectivity towards fructose, gluconic acid, arabinose and formic acid, and H_2 and CO_2 production. The listed values were obtained after 5 h of irradiation.

Photocatalyst	Conversion (%)	Selectivities (%)				H_2 [mM]	CO_2 [mM]
		Fructose	Gluconic acid	Arabinose	Formic acid		
P25	12	22	1.5	38	29	-	0.03
Pt-P25	32	31	4.6	41	31	1.93	0.07
3%Cu$_2$O-P25	28	19	8.0	30	32	1.25	0.06
Pt-BDH	21	58	4.9	-	13	1.44	0.03
Pt-Brookite	33	-	2.5	27	40	2.71	0.09
Pt-Nb1-Brookite	35	12	3.7	32	31	2.40	0.09
3%Cu$_2$O-Brookite	26	20	3.0	36	25	1.20	0.08
Pt-3%Cu$_2$O-Brookite	30	-	3.1	37	34	2.03	0.08
Pt-HP	40	27	2.6	45	44	1.89	0.14
3%Cu$_2$O-HP	37	-	3.0	49	37	1.51	0.07

Table 4. Fructose conversion, selectivity towards gluconic acid, formic acid, erythrose, and H_2 and CO_2 production. The listed values were obtained after 5 h of irradiation.

Photocatalyst	Conversion (%)	Selectivities (%)			H_2 [mM]	CO_2 [mM]
		Gluconic acid	Formic acid	Erythrose		
Pt-P25	25	9.0	12	-	3.13	0.11
3%Cu$_2$O-P25	35	5.0	5	-	1.80	0.08
Pt-BDH	28	4.1	7	-	1.34	0.02
Pt-Brookite	42	2.7	12	3.80	3.20	0.12
Pt-Nb1-Brookite	50	2.0	11	2.68	3.16	0.11
3%Cu$_2$O-Brookite	32	2.2	11	-	1.65	0.09
Pt-3%Cu$_2$O-Brookite	35	0.5	25	5.27	2.55	0.09
Pt-HP	40	4.5	6	7.47	3.26	0.12
3%Cu$_2$O-HP	35	6.2	17	7.60	1.70	0.09

Conclusions

In conclusion, the activity of various commercial and home prepared modified TiO$_2$ photocatalysts was compared for the photo-reforming of two biomass derivatives (glucose and fructose) selected as probe molecules. Numerous structural and surface characterizations have highlighted the different properties of the used samples and some of them have been related to the photocatalytic activity, although a direct correlation to a specific property was not found. This confirms the dependence of photoactivity on a number of parameters. Importantly, the home-prepared catalysts are more active than the commercial catalysts both in hydrogen generation and in the formation of partial oxidation compounds. The role of Pt in modifying the basic surface properties of the different TiO$_2$ based photocatalysts has been highlighted.

Acknowledgements

Conflict of Interest

The authors declare no conflict of interest.

References

[1]   I. Dincer, Renew. Sust. Energ. Rev. 4 (2) (2000) 157–175. https://doi.org/10.1016/S1364-0321(99)00011-8

[2]   T.G. Ambaye, M. Vaccari, A. Bonilla-Petriciolet, S. Prasad, E.D. van Hullebusch, S. Rtimi, J. Environ. Manage. 290 (1) (2021) 112627. http://doi.org/10.1016/J.JENVMAN.2021.112627

[3]   M. Bellardita, V. Loddo, L. Palmisano, Mini-Rev. Org. Chem. 17 (7) (2020) 884–901. http://doi.org/10.2174/1570193x17666200131112856

[4]   J.C. Serrano-Ruiz, R. Luque, A. Sepúlveda-Escribano, Chem. Soc. Rev. 40 (11) (2011) 5266–5281. http://doi.org/10.1039/C1CS15131B

[5]   R. Ahorsu, F. Medina, M. Constantí, Energies 11 (12) (2018). http://doi.org/10.3390/EN11123366

[6]   J. Tomaszewska, D. Bieliński, M. Binczarski, J. Berlowska, P. Dziugan, J. Piotrowski, A. Stanishevsky, I.A. Witońska, RSC Adv. 8 (6) (2018) 3161–3177. http://doi.org/10.1039/c7ra12782k

[7]   M. Ventura, A. Marinas, M.E. Domine, Top Catal. 63 (9–10) (2020) 846–865. http://doi.org/10.1007/s11244-020-01309-9

[8]   C.H. Zhou, X. Xia, C.X. Lin, D.S. Tong, J. Beltramini, Chem. Soc. Rev. 40 (11) (2011) 5588–5617. http://doi.org/10.1039/c1cs15124j

[9]   Z. Abdin, A. Zafaranloo, A. Rafiee, W. Mérida, W. Lipiński, K.R. Khalilpour, Renew. Sust. Energ. Rev. 120 (2020). http://doi.org/10.1016/J.RSER.2019.109620

[10]   P.J. Megia, A.J. Vizcaino, J.A. Calles, A. Carrero, Energy Fuels 35 (20) (2021) 16403–16415. http://doi.org/10.1021/ACS.ENERGYFUELS.1C02501

[11]   F. Qureshi, M. Yusuf, H. Kamyab, D.V.N. Vo, S. Chelliapan, S.W. Joo, Y. Vasseghian, Renew. Sust. Energ. Rev. 168 (2022) 112916. http://doi.org/10.1016/J.RSER.2022.112916

[12]   J. Esteban, P. Yustos, M. Ladero, Catalysts 8 (12) (2018) 637. http://doi.org/10.3390/catal8120637

[13]   X. Liu, X. Duan, W. Wei, S. Wang, B.J. Ni, Green Chem. 21 (16) (2019) 4266–4289. http://doi.org/10.1039/c9gc01728c

[14]   F. Guo, Z. Fang, T.J. Zhou, Bioresour. Technol. 112 (2012) 313–318. http://doi.org/10.1016/J.BIORTECH.2012.02.108

[15]   G.C. de Assis, I.M.A. Silva, T.G. dos Santos, T. V. dos Santos, M.R. Meneghetti, S.M.P. Meneghetti, Catal. Sci. Technol. 11 (7) (2021) 2354–2360. http://doi.org/10.1039/d0cy02358b

[16]   B. Ma, Y. Wang, X. Guo, X. Tong, C. Liu, Y. Wang, X. Guo, Appl. Catal. A Gen. 552 (2018) 70–76. http://doi.org/10.1016/J.APCATA.2018.01.002

[17]   Y. Zhang, S. Yang, Z. Wang, H. Qin, G. Lyu, J. Chen, G. Yang, Catal. 413 (2022) 843–857. http://doi.org/10.1016/J.JCAT.2022.07.042

[18] M. Bellardita, E.I. García-López, G. Marcì, B. Megna, F.R. Pomilla, L. Palmisano, RSC Adv. 5 (73) (2015) 59037–59047. http://doi.org/10.1039/c5ra09894g

[19] M. Bellardita, E.I. García-López, G. Marcì, G. Nasillo, L. Palmisano, Eur. J. Inorg. Chem. 2018 (41) (2018) 4522–4532. http://doi.org/10.1002/EJIC.201800663

[20] U.I. Gaya, A.H. Abdullah, J. Photochem. Photobiol. C: Photochem. Rev. 9 (1) (2008) 1–12. http://doi.org/10.1016/j.jphotochemrev.2007.12.003

[21] D. Friedmann, A. Hakki, H. Kim, W. Choi, D. Bahnemann, Green Chem. 18 (20) (2016) 5391–5411. http://doi.org/10.1039/c6gc01582d

[22] F. Parrino, M. Bellardita, E.I. García-López, G. Marcì, V. Loddo, L. Palmisano, ACS Catal. 8 (12) (2018) 11191–11225. http://doi.org/10.1021/acscatal.8b03093

[23] L. Palmisano, V. Augugliaro, M. Bellardita, A. Di Paola, E. García López, V. Loddo, G. Marcì, G. Palmisano, S. Yurdakal, ChemSusChem 4 (10) (2011) 1431–1438 http://doi.org/10.1002/cssc.201100196

[24] A. Shokri, M. Sanavi Fard, Chem. Papers 76 (35) (2022) 5309–5339. http://doi.org/10.1007/s11696-022-02256-3

[25] W.S. Koe, J.W. Lee, W.C. Chong, Y.L. Pang, L.C. Sim, Environ. Sci. Pollut. Res. 27 (3) (2020) 2522–2565. http://doi.org/10.1007/s11356-019-07193-5

[26] M. Bellardita, M. Feilizadeh, R. Fiorenza, S. Scirè, L. Palmisano, V. Loddo, Photochem. Photobiol. Sci. 21 (12) (2022). http://doi.org/10.1007/s43630-022-00284-2

[27] K. Nakata, A. Fujishima, J. Photochem. Photobiol. C: Photochem. Rev. 13 (3) (2012) 169–189. http://doi.org/10.1016/j.jphotochemrev.2012.06.001

[28] K. Hashimoto, H. Irie, A. Fujishima, J. Ind. Eng. Chem. 44 (12) (2005) 8269–8285. http://doi.org/10.1143/JJAP.44.8269

[29] H. Dong, G. Zeng, L. Tang, C. Fan, C. Zhang, X. He, Y. He, Water Res. 79 (2015) 128–146. http://doi.org/10.1016/j.watres.2015.04.038

[30] I. Arora, H. Chawla, A. Chandra, S. Sagadevan, S. Garg, Inorg. Chem. Commun. 143 (2022) 109700. http://doi.org/10.1016/J.INOCHE.2022.109700

[31] H. Tyagi, H. Chawla, H. Bhandari, S. Garg, Mater. Today Proc. 49 (2020) 3289–3305. http://doi.org/10.1016/J.MATPR.2020.12.1036

[32] R. Fiorenza, S. Sciré, L. D'Urso, G. Compagnini, M. Bellardita, L. Palmisano, Int. J. Hydrog. Energy 44 (29) (2019) 14796–14807. http://doi.org/10.1016/j.ijhydene.2019.04.035

[33] M. Bellardita, H.A.E. Nazer, V. Loddo, F. Parrino, A.M. Venezia, L. Palmisano, Catal. Today 284 (2017) 92–99. http://doi.org/10.1016/j.cattod.2016.11.026

[34] P.A. Osorio-Vargas, C. Pulgarin, A. Sienkiewicz, L.R. Pizzio, M.N. Blanco, R.A. Torres-Palma, C. Pétrier, J.A. Rengifo-Herrera, Ultrason. Sonochem. 19 (3) (2012) 383–386. http://doi.org/10.1016/j.ultsonch.2011.11.013

[35] A.M. Djaballah, M. Bellardita, L. Palmisano, V. Loddo, M. Umair, C.M. Pecoraro, R. Bagtache, M. Trari, Mol. Catal. 546 (2023) 113251. http://doi.org/10.1016/j.mcat.2023.113251

[36] C.M. Pecoraro, M. Bellardita, V. Loddo, F. Di Franco, L. Palmisano, M. Santamaria, J. Ind. Eng. Chem. 118 (2023) 247–258. http://doi.org/10.1016/j.jiec.2022.11.010

[37] J. Low, J. Yu, M. Jaroniec, S. Wageh, A.A. Al-Ghamdi, Adv. Mater. 29 (20) (2017). http://doi.org/10.1002/adma.201601694

[38] J. Duan, H. Zhao, Z. Zhang, W. Wang, Ceram. Int. 44 (18) (2018) 22748–22759. http://doi.org/10.1016/j.ceramint.2018.09.062

[39] A. Di Paola, S. Ikeda, G. Marcì, B. Ohtani, L. Palmisano, J. Photochem. Photobiol. A: Chem. 3 (2001). http://doi.org/10.1155/S1110662X01000216

[40] X. Sun, H. Liu, J. Dong, J. Wei, Y. Zhang, Catal. Lett. 135 (3–4) (2010) 219–225. http://doi.org/10.1007/s10562-010-0302-7

[41] B. Choudhury, B. Borah, A. Choudhury, Photochem. Photobiol. 88 (2) (2012) 257–264. http://doi.org/10.1111/j.1751-1097.2011.01064.x

[42] S. Ikeda, N. Sugiyama, B. Pal, G. Marcí, L. Palmisano, H. Noguchi, K. Uosaki, B. Ohtani, Phys. Chem. Chem. Phys. 3 (2) (2001) 267–273. http://doi.org/10.1039/b008028o

[43] O. Fontelles-Carceller, M.J. Muñoz-Batista, J.C. Conesa, M. Fernández-García, A. Kubacka, Appl. Catal. B 216 (2017) 133–145. http://doi.org/10.1016/J.APCATB.2017.05.022

[44] T. Ohno, M. Akiyoshi, T. Umebayashi, K. Asai, T. Mitsui, Asai, K., Mitsui, T., Matsumura, M. Appl. Catal. A Gen. 265 (1) (2004) 115–121. http://doi.org/10.1016/J.APCATA.2004.01.007

[45] R. Fiorenza, M. Bellardita, S. Scirè, L. Palmisano, Mol. Catal. 455 (2018) 108–120. http://doi.org/10.1016/j.mcat.2018.06.002

[46] F. Boccuzzi, A. Chiorino, G. Martra, M. Gargano, N. Ravasio, B. Carrozzini. J. Catal., 165 (2) (1997). http://doi.org/10.1006/jcat.1997.1475

[47] C.K. Nuo Peh, X.-Q. Wang, G.W. Ho, J. Ind. Eng. Chem. 215 (2017), 171–179. http://doi.org/10.1016/j.proeng.2017.11.006

[48] Y.H. Zhang, M.M. Liu, J.L. Chen, K.F. Xie, S.M. Fang, J. Phys. Chem. Solids 152 (2021). http://doi.org/10.1016/j.jpcs.2021.109948

[49] M.E. Aguirre, R. Zhou, A.J. Eugene, M.I. Guzman, M.A. Grela, Appl. Catal. B 217 (2017) 485–493. http://doi.org/10.1016/j.apcatb.2017.05.058

[50] M. Muscetta, R. Andreozzi, L. Clarizia, I. di Somma, R. Marotta, Int. J. Hydrog. Energy 45 (53) (2020) 28531–28552. http://doi.org/10.1016/j.ijhydene.2020.07.225

[51] M.O. Segovia-Guzmán, M. Román-Aguirre, J.Y. Verde-Gomez, V.H. Collins-Martínez, G. Zaragoza-Galán, V.H. Ramos-Sánchez, Catal. Today 349 (2020) 88–97. http://doi.org/10.1016/j.cattod.2018.05.031

[52] A. Di Paola, M. Bellardita, L. Palmisano, Catalysts 3 (1) (2013) 36–73. http://doi.org/10.3390/catal3010036

[53] A. Di Paola, G. Cufalo, M. Addamo, M. Bellardita, R. Campostrini, M. Ischia, R. Ceccato, L. Palmisano, Colloids. Surf. A Physicochem. Eng. Asp. 317 (1–3) (2008) 366–376. http://doi.org/10.1016/j.colsurfa.2007.11.005

[54]   L. Liu, H. Zhao, J.M. Andino, Y. Li, ACS Catal. 2 (8) (2012) 1817–1828.
        http://doi.org/10.1021/cs300273q

[55]   Z. Li, S. Cong, Y. Xu, ACS Catal. 4 (9) (2014) 3273–3280. http://doi.org/10.1021/cs500785z

[56]   G. Zerjav, K. Zizek, J. Zavasnik, A. Pintar, J. Environ. Chem. Eng. 10 (3) (2022).
        http://doi.org/10.1016/j.jece.2022.107722

[57]   E. Wierzbicka, M. Altomare, M. Wu, N. Liu, T. Yokosawa, D. Fehn, S. Qin, K. Meyer, T. Unruh, E.
        Spiecker, L. Palmisano, M. Bellardita, J. Will, P. Schmuki, Mater. Chem. A Mater. 9 (2) (2021)
        1168–1179. http://doi.org/10.1039/d0ta09066b

[58]   M. Bellardita, E.I. García-López, G. Marcì, L. Palmisano, Int. J. Hydrog. Energy 41 (14) (2016)
        5934–5947. http://doi.org/10.1016/j.ijhydene.2016.02.103

[59]   M.V. Dozzi, G.L. Chiarello, M. Pedroni, S. Livraghi, E. Giamello, E. Selli, Appl. Catal. B 209 (2017)
        417–428. http://doi.org/10.1016/j.apcatb.2017.03.007

[60]   J. Yu, L. Qi, M. Jaroniec, J. Phys. Chem. C 114 (30) (2010) 13118–13125.
        http://doi.org/10.1021/jp104488b

[61]   M. Muscetta, S. Al Jitan, G. Palmisano, R. Andreozzi, R. Marotta, S. Cimino, I. Di Somma, J.
        Environ. Chem. Eng. 10 (3) (2022). http://doi.org/10.1016/j.jece.2022.107735

[62]   Y. Li, B. Wang, S. Liu, X. Duan, Z. Hu, Appl. Surf. Sci. 324 (2015) 736–744.
        http://doi.org/10.1016/j.apsusc.2014.11.027

[63]   M. V. Nogueira, G.M.M.M. Lustosa, Y. Kobayakawa, W. Kogler, M. Ruiz, E.S. Monteiro Filho,
        M.A. Zaghete, L.A. Perazolli, Adv. Mater. Sci. Eng. 2018 (2018).
        http://doi.org/10.1155/2018/7326240

[64]   H.T. Kreissl, K. Nakagawa, Y.K. Peng, Y. Koito, J. Zheng, S.C.E. Tsang, J, Catal. 338 (2016) 329–
        339. http://doi.org/10.1016/j.jcat.2016.03.007

[65]   D. Maučec, A. Šuligoj, A. Ristić, G. Dražić, A. Pintar, N.N. Tušar, Catal. Today 310 (2018) 32–41.
        http://doi.org/10.1016/j.cattod.2017.05.061

[66]   V. Etacheri, C. Di Valentin, J. Schneider, D. Bahnemann, S.C. Pillai, J. Photochem. Photobiol. C:
        Photochem. Rev. 25 (2015) 1–29. http://doi.org/10.1016/J.JPHOTOCHEMREV.2015.08.003

[67]   A. Takai,,P. V. Kamat, ACS Nano 5 (9) (2011) 7369–7376. http://doi.org/10.1021/nn202294b

[68]   S. Al Jitan, Y. Li, D. Bahamon, G. Žerjav, V.S. Tatiparthi, C. Aubry, M. Sinnokrot, Z. Matouk, N.
        Rajput, M. Gutierrez, K. Al-Ali, R. Hashaikeh, A. Pintar, L.F. Vega, G. Palmisano, J. Environ.
        Chem. Eng. 11 (2) (2023). http://doi.org/10.1016/j.jece.2023.109485

[69]   N.D. Abazović, M.I. Čomor, M.D. Dramićanin, D.J. Jovanović, S.P. Ahrenkiel, J.M. Nedeljković, J.
        Phys. Chem. B 110 (50) (2006) 25366–25370. http://doi.org/10.1021/jp064454f

[70]   F. Xu, W. Xiao, B. Cheng, J. Yu, J. Int. J. Hydrog. Energy 39 (28) (2014) 15394–15402.
        http://doi.org/10.1016/j.ijhydene.2014.07.166

[71]   T. Jedsukontorn, T. Ueno, N. Saito, M. Hunsom, J. Alloys Compd. 726 (2017) 567–77.
        http://doi.org/10.1016/j.jallcom.2017.08.028

[72]   M. Bellardita, C. Garlisi, A.M. Venezia, G. Palmisano, L. Palmisano, Catal. Sci. Technol. 8 (6) (2018), 1606–1620. http://doi.org/10.1039/c7cy02382k

[73]   J.J. Murcia, M.C. Hidalgo, J.A. Navío, V. Vaiano, P. Ciambelli, D. Sannino, Int. J. Photoenergy, 2012 (2012), 687262. http://doi.org/10.1155/2012/687262

[74]   J. Yan, G. Wu, N. Guan, L. Li, Appl. Catal. B 152–153 (1) (2014) 280–288. http://doi.org/10.1016/j.apcatb.2014.01.049

[75]   J. Huo, Y. Hu, H. Jiang, C. Li, Nanoscale 6 (15) (2014) 9078–9084. http://doi.org/10.1039/c4nr00972j

[76]   S. Songtawee, B. Rungtaweevoranit, C. Klaysom, K. Faungnawakij, RSC Adv. 11 (47) (2021) 29196–29206. https://doi.org/10.1039/d1ra06002c

[77]   V.V. Kumar, G. Naresh, S. Deepa, P.G. Bhavani, M. Nagaraju, M. Sudhakar, K.V.R. Chary, A. Venugopal, J. Tardio, S.K. Bhargava, Appl. Catal. A Gen. 531 (2017) 169–176. https://doi.org/10.1016/J.APCATA.2016.10.032

[78]   M. Addamo, M. Del Arco, M. Bellardita, D. Carriazo, A. Di Paola, E. García-López, G. Marcì, C. Martín, L. Palmisano, V. Rives, Res. Chem. Intermed. 33 (3-5) (2007), 465–479. https://doi.org/10.1163/156856707779238685

[79]   M.I. Zaki, M.A. Hasan, F.A. Al-Sagheer, L. Pasupulety, Colloids Surf. A Physicochem. Eng. Asp. 190 (3) (2001), 261–274. https://doi.org/10.1016/S0927-7757(01)00690-2

[80]   L. Ding, M. Li, Y. Zhao, H. Zhang, J. Shang, J. Zhong, H. Sheng, C. Chen, J. Zhao, Appl. Catal. B: Environ. 266 (2020), 118634. https://doi.org/10.1016/j.apcatb.2020.118634

[81]   J. Zhao, Y. Wang, Y. Li, X. Yue, C. Wang. Catal. Sci. Technol. 6 (22) (2016), 7967–7975. https://doi.org/10.1039/c6cy01365a

[82]   M. Bellardita, G. Escolano-Casado, L. Palmisano, L. Mino, Catal. Today (2022), 413-415. https://doi.org/10.1016/j.cattod.2022.12.014

[83]   J.C. Colmenares, A. Magdziarz, A. Bielejewska, Bioresour. Technol. 102 (24) (2011), 11254–11257. https://doi.org/10.1016/j.biortech.2011.09.101

[84]   R. Chong, J. Li, Y. Ma, B. Zhang, H. Han, C. Li, J. Catal. 314 (2014), 101–108. https://doi.org/10.1016/j.jcat.2014.03.009

[85]   Y. Román-Leshkov, M. Moliner, J.A. Labinger, M.E. Davis, Chem. Int. Ed. 49 (47) (2010), 8954–8957. https://doi.org/10.1002/anie.201004689